Rashba spin-splitting driven inverse spin Hall effect in $MnBi_2Te_4$

Check for updates

Wen-Ti Guo [1,2], Zhigao Huang[1,2] & Jian-Min Zhang [1,2] ✉

The inverse spin Hall effect is a critical method for detecting spin Hall conductivity. Unearthing the physical relationship between electronic structure and spin Hall conductivity is conducive to establishing an intrinsic link between microstructure and macroscopic phenomena. Here, we report $MnBi_2Te_4$ as an ideal candidate: a stable, inversion symmetry-broken magnetic topological insulator for investigating the intrinsic correlation between spin Hall conductivity signal reversal and electronic structure. The valence band exhibits a significant Rashba spin splitting, with a magnitude reaching up to 4.61 eV/Å. We identify robust topological properties independent of Rashba and Lifshitz spin-splitting types. Moreover, transitioning the spin-splitting type not only widens the bulk band gap, enhancing the spin Hall conductivity plateau, but also triples the intrinsic spin Hall conductivity value. We propose the inverse spin Hall effect that is tunable by spin-splitting types, thereby advancing the research on the microscopic electronic mechanisms of spin current detection.

Extensive research has focused on the detection of spin currents facilitated by the inverse spin Hall effect (ISHE) for the spin-charge conversion[1–6]. The compensated magnetism of antiferromagnets supports only spin-neutral currents, making the generation and detection of spin currents challenging[7–9]. The realization of the ISHE is of significant importance for the detection of spin currents. However, the microscopic physical mechanisms of ISHE are still unclear, which greatly impedes further understanding of the physical origins of ISHE.

ISHE is intrinsically linked to spin–orbit coupling (SOC), and investigating SOC is instrumental for a deeper understanding of ISHE. By modulating the Berry curvature, a sign inversion of the spin Hall conductivity (SHC) can be induced, see Supplementary Note 1. Vardeny et al. discovered the ISHE in organic semiconductors with tunable SOC[1]. SOC manipulates electron spins without an external magnetic field, crucial for advancements in spintronics and the spin Hall effect (SHE)[10]. Systems with microscopic electric fields exhibit bulk inversion asymmetry and structural inversion asymmetry (SIA), leading to Dresselhaus and Rashba interactions. Crystalline materials leveraging Rashba[11] and Dresselhaus[12] SOC generate momentum-dependent spin–orbit fields, disrupting original spin state degeneracy and creating complex spin configurations.

Rashba SOC, with its linear wave vector k, produces concentric circular Fermi surfaces and distinct chiral spin textures, as shown in Supplementary Note 2. Introducing a nonlinear Rashba term generates out-of-plane spin texture[13–17]. The spin texture modulates zero-field spin–orbit torque in vertically magnetized systems[18], enabling the exploration of transport phenomena like intrinsic SHE[19–21], spin supercurrent in superconductors[22], anomalous Hall effect[23], spin-to-charge conversion, and nonlinear transport effects[24]. The substantial Rashba effect serves as an effective remedy for enhancing the efficiency of spin-to-charge current conversion, which is imperative for the design of high-conversion efficiency spintronic devices that do not require the influence of an external magnetic field. The rare Rashba effect observed in the 3D bulk system[25] will significantly facilitate the design and application of non-volatile memory components and logic computation.

Here, we will unveil the substantial Rashba spin-splitting hidden within the antiferromagnetic (AFM) bulk structure of the intrinsic magnetic topological insulator $MnBi_2Te_4$ and its physical correlation with the ISHE. Firstly, we conduct a computational assessment of the substantial Rashba splitting, polarization, and structural stability of the $MnBi_2Te_4$ with broken $\mathcal{I}$-symmetry. In addition, by transforming the type of spin-splitting, we will significantly enhance the SHC and induce the ISHE. Concurrently, we further explore the relationship between the ISHE phenomenon and the spin distribution across the energy bands. Furthermore, by constructing an effective model, we will provide a rational explanation for the mechanism of Rashba spin-splitting in $MnBi_2Te_4$, emphasizing the robustness of the system's topological properties in response to variations in spin-splitting.

[1]Fujian Provincial Key Laboratory of Quantum Manipulation and New Energy Materials, College of Physics and Energy, Fujian Normal University, Fuzhou, 350117, China. [2]Fujian Provincial Collaborative Innovation Center for Advanced High-Field Superconducting Materials and Engineering, Fujian Normal University, Fuzhou, 350117, China. ✉e-mail: jmzhang@fjnu.edu.cn

Results and discussion

Physical depiction of ISHE

We first propose a corresponding physical depiction for how to achieve the ISHE in Supplementary Note 1. As shown in Fig. 1, the observed SHC reversal can be attributed to changes in spin-splitting and spin distribution within the energy band. Considering the charge current j_C^z in the out-of-plane z direction, it generates spin currents j_x^{zy} along the $+x$ direction and j_y^{sx} along the $-y$ direction in the xz and yz planes, respectively. The MnBi$_2$Te$_4$ system with broken $\mathcal{I}$ symmetry is used to achieve ISHE, resulting in non-zero SHC values such as σ_{xz}^y and σ_{yz}^x in these planes. In Rashba splitting, $\sigma_{xz}^y < 0$ and $\sigma_{yz}^x > 0$, whereas in Lifshitz splitting, the pattern reverses. In contrast to Rashba splitting, which has only one valence band peak, Lifshitz splitting, arising from the phenomenon of Lifshitz transition, exhibits two peak values in both valence bands[26]. The reversal in the SHC sign is closely tied to the transition of bulk energy bands from Rashba-type splitting to Lifshitz-type splitting.

In addition, the evolution of spin distributions during this transition is further explored. For example, along the K-Γ-K_2 path, the spin orientations of the two valence bands near the Fermi level shift from a simple $<\uparrow\downarrow\uparrow\downarrow>$ in Rashba-type splitting to a more intricate $<\uparrow\uparrow\downarrow\downarrow>$ in Lifshitz-type splitting. This change in spin distribution may be due to external factors like pressure, which compresses the bulk energy band and results in two distinct energy band peaks in a Lifshitz-type splitting. As the second-highest occupied valence band moves upward, the spin orientation changes regularly, subsequently influencing the SHC. We establish a direct link between observations of spin currents and the nature of energy band spin-splitting. Many studies have detailed methods for detecting spin currents[2,3,7–9,27–35], and our approach of linking ISHE with spin distribution will aid in this detection.

Experimentally, the direction of the spin current can be predicted based on the valence band features (Rashba or Lifshitz splitting) observed near the Fermi level through angle-resolved photoemission spectroscopy (ARPES), providing crucial insights into the challenging observation of SHC in AFM systems. The occurrence of Lifshitz transitions can be confirmed experimentally by observing changes in Fermi surface features under temperature control[36–38], chemical doping or substitution[39,40], or applied pressure[41,42] through ARPES. For example, Zhang et al. observed a Lifshitz transition in the topological insulator ZrTe$_5$ through ARPES, where the Fermi surface at the Γ point evolved from a hole pocket to an electron pocket under temperature variation. Here, we focus on the R-MBT system with inversion symmetry breaking to study the SHC properties during the transition from Rashba to Lifshitz spin-splitting. It is worth noting that, although early studies based on group theory have proposed such inversion symmetry-breaking structures for MnBi$_2$Te$_4$[43], further experimental investigations (e.g., high-resolution transmission electron microscopy (TEM) or local scanning tunneling microscopy (STM)) are still needed to reveal the potential Te sublattice displacement structure.

Structure and symmetry

The typical MnBi$_2$Te$_4$ configuration consists of a principal van der Waals hexagonal phase layered structure within the D_{3d}^5 (No. 166) space group[44]. In nonmagnetic ordering, MnBi$_2$Te$_4$ exhibits mirror symmetry M_x, three-fold rotation symmetry C_{3z}, $\mathcal{I}$, and time-reversal symmetry $\mathcal{T}$. The AFM-z ordering disrupts the M_x and $\mathcal{T}$ symmetries but is preserved by the combined symmetry $S = \mathcal{T}\tau_{1/2}$, where $\tau_{1/2}$ denotes half-lattice translational symmetry. As shown in Fig. 2a, the MnBi$_2$Te$_4$ SL connects two Bi-Te octahedral layers, Layer1 and Layer2, with the Mn atomic layer serving as the inversion center, maintaining $\mathcal{I}$ symmetry. Introducing appropriate lattice shifts to the Te atomic layer at the octahedral layer edges results in the violation of $\mathcal{I}$ symmetry, transforming MnBi$_2$Te$_4$ from the $R\bar{3}m$ phase to the $P3m1$ (C_{3v}) phase (referred to as R-MBT), as shown in Fig. 2b. R-MBT structure was also achieved in a previous study by altering the layer stacking pattern of MnBi$_2$Te$_4$[43]. The correspondence between the representations of

D_{3d} and C_{3v} can be expressed as $D_{3d} \rightarrow C_{3v}$: $A_{1i} \rightarrow A_1$, $A_{2i} \rightarrow A_2$, $E_i \rightarrow E$ ($i = g, u$)[45], outlining the symmetry-breaking process driven by interlayer displacement.

Polarization feature and stability

In R-MBT, polarization is typically induced by the SIA. The polarization in AFM-ordered R-MBT is comparable to materials like BaTiO$_3$[46] and HfO$_2$ in the $Pca2_1$ and $Pmn2_1$ phases[47], as detailed in Supplementary Note 3. Like the pyroelectric material CaBaCo$_4$O$_7$[48–50], the polarization in R-MBT can be tuned by controlling magnetic order. Phonon spectrum calculations confirm the stability of R-MBT, as shown in Fig. 2c, alongside the projection of bulk bands from the A-type AFM MnBi$_2$Te$_4$. Near the Γ point, the energy band inversion indicates topological nontriviality, with Rashba spin-splitting as a prominent feature.
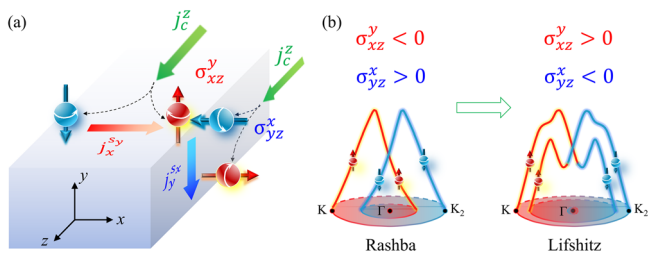
Rashba spin-splitting

The spin-splitting phenomenon in this stable system with polarization is quite pronounced. In R-MBT, the conduction and valence bands near the Fermi level exhibit significant Rashba splitting, with $\alpha_R^{VBM} = 4.631$ eVÅ and $\alpha_R^{CBM} = 4$ eVÅ, surpassing BiTeI[51] and comparable to systems like PtBi$_2$, KSnSb$_x$Bi$_{1-x}$, and others[52–54], as detailed in Supplementary Note 4. Figure 3a, b show Rashba and Lifshitz band spin-splittings, which can transition by altering Rashba strength. Fermi surfaces in Fig. 3c, d also confirm Rashba splitting. The robust Rashba splitting is evident from the C_{3z} rotational symmetry and alternating chirality in the Fermi morphology and spin texture at different energy cross-sections, as shown in Fig. 3e–g and Supplementary Fig. S2. It is noteworthy that when the spin-splitting changes from Rashba to Lifshitz, the chirality of the highest pair of valence bands transitions from the opposite (see Fig. 3e) to the same (see Supplementary Fig. S3 at the energy cut $E_F - 0.175$). The physical essence of this change in chirality is induced by the redistribution of spin caused by the deformation of the compressed band structure, see Supplementary Note 5. Despite the bulk bandgap opening in R-MBT due to layer dislocations, a topological surface state ensures an isotropic helical spin texture at the Fermi level, as shown in Fig. 3f. At the ($E_F + 0.1$) and ($E_F - 0.12$) eV cross-sections, the nested bands exhibit spin textures with opposite chirality, reaffirming the presence of Rashba spin-splitting. These computational findings are instrumental in guiding experimental observations and are likely to yield comparable ARPES results. We attribute the physical origin of the Rashba spin-splitting to the intrinsic electric field induced by the electrostatic potential differences between atoms.

Effective model construction

To understand how structural $\mathcal{I}$ breaking triggers Rashba band spin-splitting in MnBi$_2$Te$_4$, we developed tight-binding (TB) and $\mathbf{k} \cdot \mathbf{p}$ models to reproduce the energy band profiles from density functional theory (DFT) calculations, as detailed in Supplementary Notes 6, 7. The constructed TB model primarily relies on nearest-neighbor hopping parameters t_l ($l = 1$–4) and next-nearest-neighbor parameters r_1, r_3. The imaginary terms t_1 and r_1 play a major role in achieving spin splitting, while t_2, t_3, and r_3 significantly influence the degree of splitting, as detailed in Supplementary Note 7.

Based on system symmetry, the $\mathbf{k} \cdot \mathbf{p}$ model for the R-MBT system has been meticulously constructed. The magnetic space group of the A-type AFM configuration is P_c3c1 (MSG = 158.60). The system's 12 symmetry operations include six under time reversal, encompassing the identity matrix E, out-of-plane triple rotational symmetries C_{3z}^+ and C_{3z}^-, and in-plane mirror symmetries M_{100}, M_{010}, and M_{110}. The energy bands near the Fermi level unfold at the Γ point as a double Γ_4. The conduction and valence band Hamiltonians are derived in Supplementary equation S12 under the Γ_4 unitary operation C_{3z}^+, M_{100}, and the anti-unitary transformation $E|00\frac{1'}{2}$. These $\mathbf{k} \cdot \mathbf{p}$ model Hamiltonians convert efficiently into a Pauli matrix representation, as shown in Eq. (1), with

$\Gamma_{i,j} = \sigma_i \otimes \sigma_j$ ($i, j = 0, 1, 2, 3$), where σ_i and σ_j are Pauli matrices. Furthermore, based on Supplementary equation S12, the Hamiltonian of the R-MBT system is primarily modulated by the constant terms $C_{0,i}$ ($i = 1$–4), first-order terms $C_{1,j}(j = 2, 3, 4)$, and second-order terms $C_{2,k}(k = 6, 7, 8)$. The imaginary coefficient $C_{2,6}$ is crucial for inducing Rashba splitting, which will become zero in Lifshitz-type splitting; however, Lifshitz-type splitting will increase the coefficient $C_{2,7}$ associated with the term $k_x^2 + k_y^2$. Fine-tuning specific parameters aligns the energy band structure with DFT calculations. For Rashba-type splitting, parameters are $C_{0,1} = 0.0578$, $C_{0,2} = 0.0252$, $C_{0,3} = -0.0045$, $C_{1,2} = 0.1$, $C_{1,3} = 0.0248$, $C_{2,6} = 0.004$, $C_{2,8} = 0.0105$, with others set to zero. For Lifshitz-type splitting, parameters are adjusted to $C_{0,2} = 0$, $C_{1,2} = -0.01$, $C_{1,3} = 0.05$, $C_{1,4} = -0.045$, $C_{2,7} = -0.06$, $C_{2,8} = 0.03$. The energy band results from TB and $\mathbf{k} \cdot \mathbf{p}$ models are compared with DFT calculations as
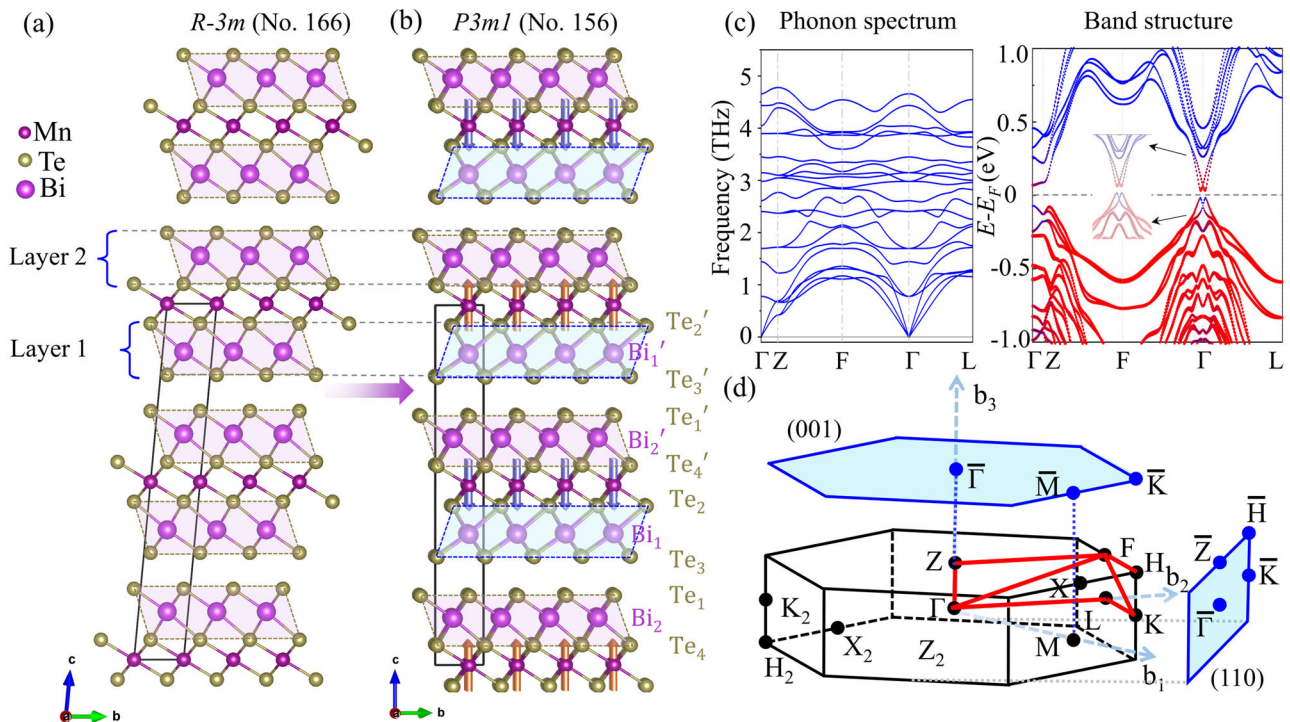
presented in Supplementary Fig. S5.

$$\begin{aligned}
\mathcal{H}(k) = &(C_{0,3} + C_{2,3}k_z^2 + C_{2,8}(k_x^2 + k_y^2))\Gamma_{0,0} \\
&+ C_{1,4}k_y\Gamma_{0,1} + C_{1,4}k_x\Gamma_{0,3} \\
&+ (C_{0,2} + C_{2,2}k_z^2 + C_{2,7}(k_x^2 + k_y^2))\Gamma_{1,0} \\
&+ C_{1,3}k_y\Gamma_{1,1} + C_{1,3}k_x\Gamma_{1,3} + C_{1,1}k_z\Gamma_{2,0} \\
&+ (C_{2,4}k_yk_z + 2C_{2,6}k_xk_y)\Gamma_{2,1} \\
&+ (C_{2,4}k_xk_z - C_{2,6}(k_x^2 - k_y^2))\Gamma_{2,3} \\
&+ (C_{0,1} + C_{2,1}k_z^2 + C_{2,5}(k_x^2 + k_y^2))\Gamma_{3,0} \\
&+ C_{1,2}k_y\Gamma_{3,1} + C_{1,2}k_x\Gamma_{3,3}
\end{aligned} \tag{1}$$

Topological properties and SHC

The Rashba SOC exerts a profound influence on the topological properties and the quantum spin Hall effect of topological insulators, with its potential to facilitate dissipationless spin currents in quantum computing being particularly remarkable. To further investigate the topological properties and SHC of the R-MBT system, the (110) planes of both types of spin-splitting have gapless topological surface states protected by the S symmetry (see Fig. 4). Both types of spin-splitting exhibit topological properties with $Z_2 = 1$. Unlike Rashba splitting, Lifshitz splitting has identical left and right terminal surface states on the (110) plane. In the (001) plane, surface states clearly demonstrate the differences between the two types of spin-splitting in the valence band, with a significant surface bandgap in one terminal state. Transforming Rashba-type splitting into Lifshitz-type splitting results in a larger surface bandgap in the (001) plane.

The crystalline structure of R-MBT belongs to the $3m1'$ magnetic point group, with three sets of non-zero SHC tensor elements, $\sigma_{\beta\gamma}^{\alpha}$, where α, β, and γ can be x, y, or z. These elements describe the spin current's polarization along α and the spin current in β induced by an electric field in γ. The SHC of R-MBT reveals relationships like $\sigma_{yz}^x = -\sigma_{xz}^y$, $\sigma_{zx}^y = -\sigma_{zy}^x$, and $\sigma_{xy}^z = -\sigma_{yx}^z$,

Fig. 1 | The physical correlation between spin Hall conductivity (SHC), spin-splitting types, and spin distribution. a Schematic diagram illustrating the relationship between electron spin orientation, spin current, and charge current in SHC devices. **b** SHC signals as a function of the type of spin-splitting (Rashba and Lifshitz) and spin distribution in the band structure. The $\vec{j}_C^z$ represents the charge current in the z direction. And j_x^{sy} and j_y^{sx} denote the spin currents along the x and y orientations, respectively, where s_y and s_x indicate the spin directions. In the SHC $\sigma_{\beta\gamma}^{\alpha}$, α, β, and γ correspond to the directions of spin, spin current, and charge current, which can be arranged in any combination of x, y, and z.

Fig. 2 | Crystal structure, band structure, and the first Brillouin zone. MnBi$_2$Te$_4$ with **a** $R\bar{3}m$ space group and **b** $P3m1$ space group. **c** Phonon spectrum and projected energy band structure, containing an inset image of MnBi$_2$Te$_4$ with the $P3m1$ space

group (where blue and red represent Bi-p and Te-p orbital contributions, respectively). **d** First Brillouin zone with the projections of (001) and (110) planes.
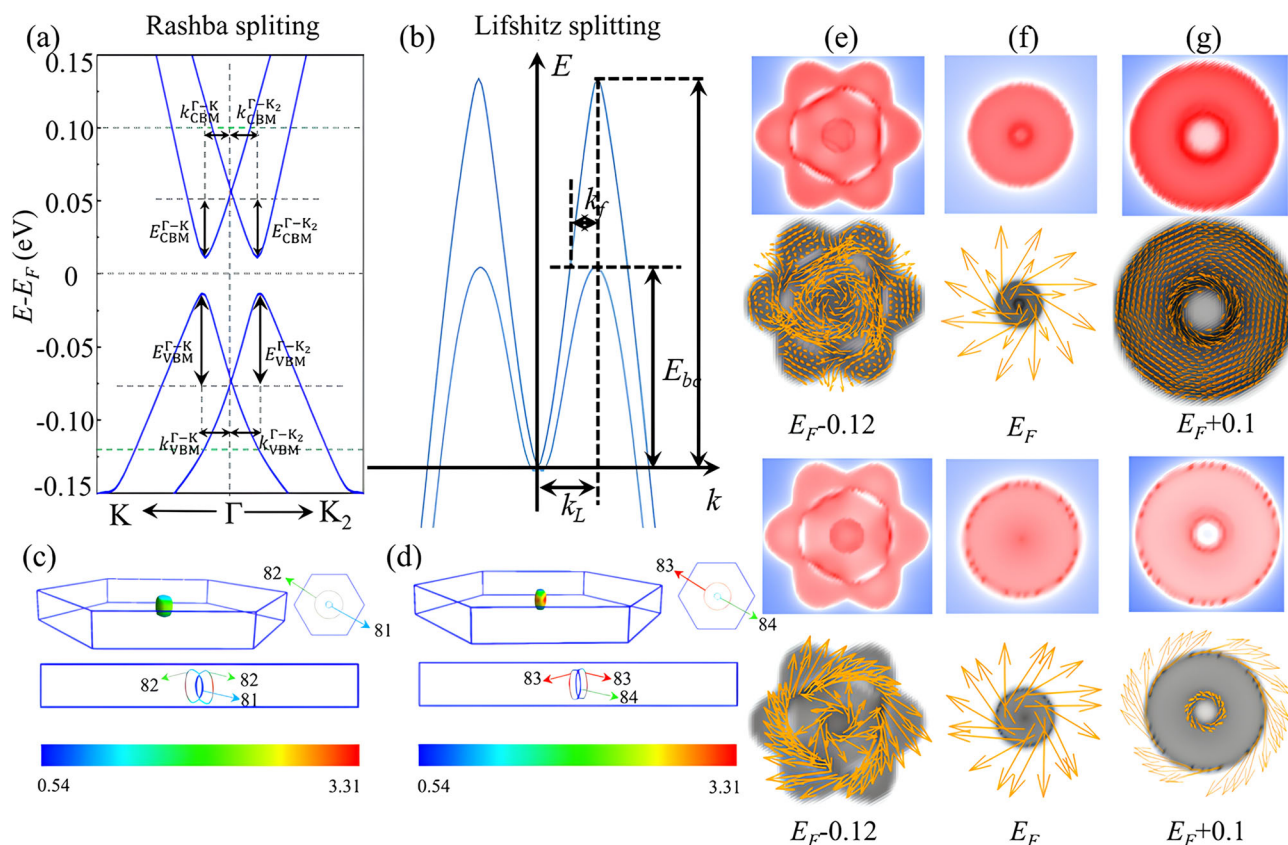
Fig. 3 | Schematic diagrams of two spin-splitting types and evidence of Rashba splitting. a Rashba and **b** Lifshitz band splits. Momentum $k_{\text{CBM, VBM}}^{\Gamma-k,\Gamma-k_2}$, k_f, k_L and energy $E_{\text{CBM, VBM}}^{\Gamma-k,\Gamma-k_2}$, E_{bc} dependent on specific paths for conduction band minimum (CBM) and valence band maximum (VBM). Fermi surface of the Rashba splitting band on **c** valence band (81 and 82) **d** conduction band (83 and 84). The color bar reflects the Fermi velocity values, with red indicating the maximum and blue indicating the minimum. Fermi surface and Spin textures under different energy cross-sections, which are **e** $(E_F - 0.12)$, **f** (E_F), and **g** $(E_F + 0.1)$ eV (each cross section is marked with a dashed line in 3a).
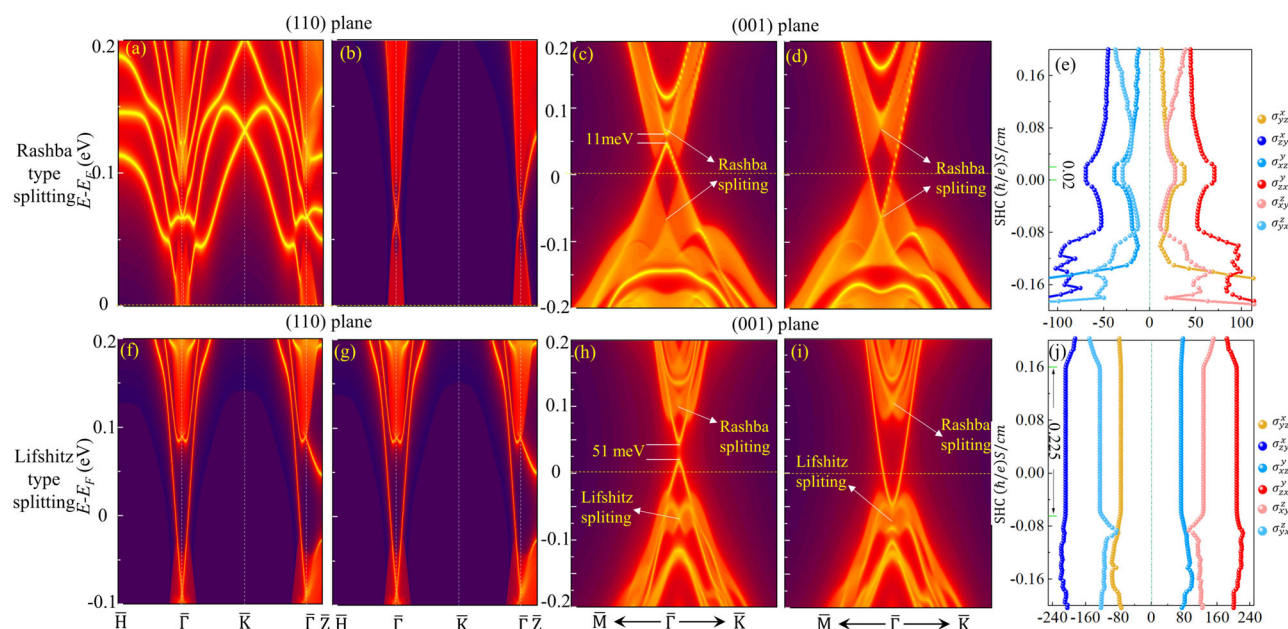
Fig. 4 | Topological surface states and SHC components of the two splitting types. Surface states and SHC of **a–e** Rashba-type and **f–j** Lifshitz-type energy band splits. From left to right, the left and right terminal surface states of the (110) and (001) planes, respectively, and the SHC in each direction.

shown in Fig. 4e, j. At the Fermi level, the highest SHC values for Rashba-type and Lifshitz-type spin-splittings are $\sigma_{zx}^{y}=-\sigma_{zy}^{x}=70$ ($\hbar$ Se^{-1}cm^{-1}) and 208 ($\hbar$ Se^{-1}cm^{-1}), respectively. While the SHC of R-MBT is lower than that of Pt (2280 ($\hbar$ Se^{-1}cm^{-1}), it is closer to α-Ta (-142) and β-Ta (-389)[55]. The intrinsic SHC near the Fermi level of the topological insulator (Bi/Sb)$_2$ (Te/Se)$_3$ ranges between 50 and 100 ($\hbar$ Se^{-1}cm^{-1}), with spin torque levels comparable to those of surface interaction[56]. Transitioning from Rashba-type to Lifshitz-type spin-splitting reverses the signs of SHCs σ_{yz}^{x} and σ_{xz}^{y}. We propose an ISHE with SHC sign reversal, explained in Fig. 1. Meanwhile, the behavior of the sum of Berry curvature, which reverses orientation after the transition of the splitting type, is shown in Supplementary Fig. S7.

Conclusion

We propose a theoretical ISHE phenomenon dependent on spin distribution and spin-splitting type, identifying MnBi$_2$Te$_4$ as an ideal material to observe this effect. Firstly, we attribute the SHC sign-reversal to changes in spin distribution, induced by the competition between opposite spin components within the same energy band under an external field. Then, it reveals significant Rashba spin-splittings of up to 4 eVÅ and 4.61 eVÅ in the conduction and valence bands of R-MBT, respectively. Next, we identified an electric polarization of up to 0.51 C per m^2 in R-MBT with both in-plane and out-of-plane linear AFM ordering, and up to 0.37 C per m^2 with linear ferromagnetic ordering. This polarization remains consistent regardless of magnetic ordering orientation. The phonon dispersion spectrum confirms the stability of the R-MBT system. Additionally, Rashba splitting is substantiated through analysis of Fermi surface morphology and spin textures across various energy cross-sections. Moreover, symmetry analyses and calculations allowed us to establish TB and $\mathbf{k} \cdot \mathbf{p}$ models for the R-MBT system. Our investigations indicate that the system retains non-trivial topological properties as Rashba splitting transforms into Lifshitz splitting, manifesting gapless topological surface states in specific planes safeguarded by S symmetry. Finally, the conversion of band splitting type significantly broadens the SHC platform, profoundly influencing the system's transport behavior. Importantly, the non-zero SHCs from in-plane spin currents j_x^{sy} and j_y^{sx}, induced by the out-of-plane charge current j_C^z, exhibit an inverse relationship with changes in spin-splitting type.

Methods

First-principles calculations were done using Vienna *ab* initio simulation package[57,58], with projector augmented-wave[59] and a Perdew–Burke–Ernzerh-type generalized gradient approximation function[60]. The truncation energy of the plane wave basis is set to 350 eV. The SOC is taken into account in all our calculations. the Monkhorst–Pack *k*-point grid centered on Γ is set to $9 \times 9 \times 3$. The software[61–63] used for post-processing calculations is detailed in Supplementary Methods.

Supplementary information. The definitions of spin Hall conductivity, origins of Rashba SOC, calculation details, and analyses of polarization, Rashba splitting, berry curvature, and spin distribution, as well as the construction of the TB and k · p models.

Data availability

The datasets generated and/or analyzed during the current study are available in the Figshare https://doi.org/10.6084/m9.figshare.27979445. Further requests can be made to the corresponding author upon reasonable request.

References

1. Sun, D. et al. Inverse spin Hall effect from in organic semiconductors with tunable spin-orbit coupling. *Nat. Mater.* **15**, 863–869 (2016).
2. Wu, H. et al. Observation of pure inverse spin hall effect in ferromagnetic metals via ferromagnetic/antiferromagnetic exchange-bias structures. *Phys. Rev. B* **92**, 054404 (2015).
3. Hoque, A. M., Khokhriakov, D., Karpiak, B. & Dash, S. P. Charge-spin conversion in layered semimetal TaTe$_2$ and spin injection in van der waals heterostructures. *Phys. Rev. Res.* **2**, 033204 (2020).
4. Wang, Z. Q. et al. Inverse spin Hall effect dominated spin-charge conversion in (101) and (110)-oriented RuO$_2$ films. *Phys. Rev. Lett.* **133**, 046701 (2024).
5. Liao, C.-T., Wang, Y.-C. & Tien, Y.-C. et al. Separation of inverse alternmagnetic spin-splitting effect from inverse spin hall effect in ruo$_2$. *Phys. Rev. Lett.* **133**, 056701 (2024).
6. Kamra, L. J. & Linder, J. Inverse spin-hall effect and spin swapping in spin-split superconductors. *Phys. Rev. Lett.* **132**, 226002 (2024).
7. Nichele, F. et al. Generation and detection of spin currents in semiconductor nanostructures with strong spin-orbit interaction. *Phys. Rev. Lett.* **114**, 206601 (2015).
8. Huang, L. et al. Antiferromagnetic inverse spin hall effect. *Adv. Mater.* **34**, 2205988 (2022).
9. Shao, D.-F. et al. Néel spin currents in antiferromagnets. *Phys. Rev. Lett.* **130**, 216702 (2023).
10. Manchon, A., Koo, H. & Nitta, J. et al. New perspectives for Rashba spin-orbit coupling. *Nat. Mat.* **14**, 871–882 (2015).
11. Rashba, E. Properties of semiconductors with an extremum loop. I. Cyclotron and combinational resonance in a magnetic field perpendicular to the plane of the loop. *Sov. Phys. Solid State* **2**, 1109 (1960).
12. Dresselhaus, G. Spin-orbit coupling effects in zinc blende structures. *Phys. Rev.* **100**, 580–586 (1955).
13. Xie, R. et al. Three-dimensional rashba spin splitting dominated by out-of-plane spin polarization. *Phys. Rev. B* **107**, 155436 (2023).
14. Absor, M. A. U. & Ishii, F. Intrinsic persistent spin helix state in two-dimensional group-IV monochalcogenide *MX* monolayers ($M =$ Sn or Ge and $X =$, Se, or Te). *Phys. Rev. B* **100**, 115104 (2019).
15. Sasmito, S. A., Anshory, M., Jihad, I. & Absor, M. A. U. Reversible spin textures with giant spin splitting in two-dimensional Ga*XY* ($X =$ Se, Te; $Y =$ Cl, Br, I) compounds for a persistent spin helix. *Phys. Rev. B* **104**, 115145 (2021).
16. Absor, M. A. U. & Santoso, I. Reversible canted persistent spin textures in two-dimensional ferroelectric bilayer WTe$_2$. *J. Appl. Phys.* **132**, 183906 (2022).
17. Absor, M. A. U. et al. Highly persistent spin textures with giant tunable spin splitting in the two-dimensional germanium monochalcogenides. *J. Phys. Condens. Mat.* **33**, 305501 (2021).
18. Mengxi, W. et al. Field-free spin-orbit torque switching via out-of-plane spin-polarization induced by an antiferromagnetic insulator/heavy metal interface. *Nat. Commun.* **14**, 2871 (2023).
19. Peng, S. et al. Coexistence of large conventional and planar spin Hall effect with long spin diffusion length in a low-symmetry semimetal at room temperature. *Nat. Mater.* **19**, 292–298 (2020).
20. Vila, M. et al. Low-symmetry topological materials for large charge-to-spin interconversion: the case of transition metal dichalcogenide monolayers. *Phys. Rev. Res.* **3**, 043230 (2021).
21. Abanin, D. A., Lee, P. A. & Levitov, L. S. Charge and spin transport at the quantum Hall edge of graphene. *Solid State Commun.* **143**, 77–85 (2007).
22. He, J. J., Hiroki, K., Hamamoto, K. & Nagaosa, N. Spin supercurrent in two-dimensional superconductors with Rashba spin-orbit interaction. *Commun. Phys.* **2**, 128 (2019).
23. Yoo, M.-W. et al. Large intrinsic anomalous Hall effect in SrIrO$_3$ induced by magnetic proximity effect. *Nat. Commun.* **12**, 3283 (2021).
24. Bihlmayer, G., Noel, P., Vyalikh, D. V., Chulkov, E. & Manchon, A. Rashba-like physics in condensed matter. *Nat. Rev. Phys.* **4**, 642–659 (2022).
25. Dettwiler, F. et al. Stretchable persistent spin helices in GaAs quantum wells. *Phys. Rev. X* **7**, 031010 (2017).
26. Li, P. et al. Biaxial strain modulated electronic structures of layered two-dimensional MoSiGeN$_4$ Rashba systems. *Phys. Chem. Chem. Phys.* **26**, 1891–1903 (2024).
27. Yuan, W., Li, J. & Shi, J. Spin current generation and detection in uniaxial antiferromagnetic insulators. *Appl. Phys. Lett.* **117**, 100501 (2020).

28. Kukreja, R. et al. X-ray detection of transient magnetic moments induced by a spin current in Cu. *Phys. Rev. Lett.* **115**, 096601 (2015).

29. Arakawa, N. & Yonemitsu, K. Symmetry-protected difference between spin Hall and anomalous Hall effects of a periodically driven multiorbital metal. *Commun. Phys.* **6**, 43 (2023).

30. Das, K. S., Liu, J., van Wees, B. J. & Vera-Marun, I. J. Efficient injection and detection of out-of-plane spins via the anomalous spin Hall effect in permalloy nanowires. *Nano Lett.* **18**, 5633–5639 (2018).

31. Camosi, L. et al. Resolving spin currents and spin densities generated by charge-spin interconversion in systems with reduced crystal symmetry. *2D Mater.* **9**, 035014 (2022).

32. Werake, L. K. & Zhao, H. Observation of second-harmonic generation induced by pure spin currents. *Nat. Phys.* **6**, 875–878 (2010).

33. Miah, M. I. Generation and detection of spin current in semiconductors: semiconductor spintronics. *Mater.* **2**, 5111–5116 (2015).

34. Gunnink, P. M., Duine, R. A. & Rückriegel, A. Electrical detection of unconventional transverse spin currents in obliquely magnetized thin films. *Phys. Rev. B* **101**, 220407 (2020).

35. Yang, X., van der Wal, C. H. & van Wees, B. J. Detecting chirality in two-terminal electronic nanodevices. *Nano Lett.* **20**, 6148–6154 (2020).

36. Wu, Y. et al. Temperature-induced Lifshitz transition in WTe_2. *Phys. Rev. Lett.* **115**, 166602 (2015).

37. Yang, M. et al. Large-gap quantum spin Hall state and temperature-induced Lifshitz transition in Bi_4Br_4. *ACS Nano* **16**, 3036–3044 (2022).

38. Zhang, Y. et al. Electronic evidence of temperature-induced Lifshitz transition and topological nature in $ZrTe_5$. *Nat. Commun.* **8**, 15512 (2017).

39. Liu, C. et al. Importance of the Fermi-surface topology to the superconducting state of the electron-doped pnictide $Ba(Fe_{1-x}Co_x)_2As_2$. *Phys. Rev. B* **84**, 020509 (2011).

40. Liu, C. et al. Evidence for a Lifshitz transition in electron-doped iron arsenic superconductors at the onset of superconductivity. *Nat. Phys.* **6**, 419–423 (2010).

41. Kang, D. et al. Superconductivity emerging from a suppressed large magnetoresistant state in tungsten ditelluride. *Nat. Commun.* **6**, 7804 (2015).

42. Bud'ko, S., Voronovskii, A., Gapotchenko, A. & Itskevich, E.-S. The fermi surface of cadmium at an electron-topological phase transition under pressure. *Zh. Eksp. Teor. Fiz.* **86**, 778 (1984).

43. Rodriguez-Vega, M., Leonardo, A. & Fiete, G. A. Group theory study of the vibrational modes and magnetic order in the topological antiferromagnet $Mnbi_2te_4$. *Phys. Rev. B* **102**, 104102 (2020).

44. Zhang, D. et al. Topological axion states in the magnetic insulator $MnBi_2Te_4$ with the quantized magnetoelectric effect. *Phys. Rev. Lett.* **122**, 206401 (2019).

45. Aroyo, M. I., Kirov, A., Capillas, C., Perez-Mato, J. M. & Wondratschek, H. Bilbao crystallographic server. II. Representations of crystallographic point groups and space groups. *Acta Crystallogr. A* **62**, 115–128 (2006).

46. Wieder, H. H. Electrical behavior of barium titanatge single crystals at low temperatures. *Phys. Rev.* **99**, 1161–1165 (1955).

47. Huan, T. D., Sharma, V., Rossetti, G. A. & Ramprasad, R. Pathways towards ferroelectricity in hafnia. *Phys. Rev. B* **90**, 064111 (2014).

48. Dhanasekhar, C. et al. Switching from pyroelectric to ferroelectric order in Ni-doped $CaBaCo_4O_7$. *Phys. Rev. B* **96**, 134413 (2017).

49. Fishman, R. S. et al. Competing exchange interactions in multiferroic and ferrimagnetic $CaBaCo_4O_7$. *Phys. Rev. B* **95**, 024423 (2017).

50. Johnson, R. D., Cao, K., Giustino, F. & Radaelli, P. G. $CaBaCo_4O_7$: a ferrimagnetic pyroelectric. *Phys. Rev. B* **90**, 045129 (2014).

51. Ishizaka, K., Bahramy, M. S., Murakawa, H. & Sakano, M. Giant Rashba-type spin splitting in bulk BiTeI. *Nat. Mater.* **10**, 521–526 (2011).

52. Mondal, C., Barman, C. K., Alam, A. & Pathak, B. Intertwined nontrivial band topology and giant rashba spin splitting. *Phys. Rev. B* **104**, 085113 (2021).

53. Mera Acosta, C., Ogoshi, E., Fazzio, A., Dalpian, G. M. & Zunger, A. The Rashba scale: emergence of band anti-crossing as a design principle for materials with large rashba coefficient. *Matter* **3**, 145–165 (2020).

54. Gupta, S. K., Kore, A., Sen, S. K. & Singh, P. Coexistence of giant Rashba splitting, multiple band inversion, and multiple Dirac surface states in the three-dimensional topological insulator $XSnBi(X=Rb, Cs)$. *Phys. Rev. B* **107**, 075143 (2023).

55. Qiao, J., Zhou, J., Yuan, Z. & Zhao, W. Calculation of intrinsic spin hall conductivity by Wannier interpolation. *Phys. Rev. B* **98**, 214402 (2018).

56. Farzaneh, S. M. & Rakheja, S. Intrinsic spin hall effect in topological insulators: a first-principles study. *Phys. Rev. Mater.* **4**, 114202 (2020).

57. Kresse, G. & Hafner, J. ab initio molecular dynamics for open-shell transition metals. *Phys. Rev. B* **48**, 13115–13118 (1993).

58. Kresse, G. & Furthmüller, J. Efficient iterative schemes for ab initio total-energy calculations using a plane-wave basis set. *Phys. Rev. B* **54**, 11169–11186 (1996).

59. Blöchl, P. E. Projector augmented-wave method. *Phys. Rev. B* **50**, 17953–17979 (1994).

60. Perdew, J. P., Burke, K. & Ernzerhof, M. Generalized gradient approximation made simple. *Phys. Rev. Lett.* **77**, 3865–3868 (1996).

61. Wu, Q., Zhang, S., Song, H.-F., Troyer, M. & Soluyanov, A. A. Wanniertools: an open-source software package for novel topological materials. *Comput. Phys. Commun.* **224**, 405–416 (2018).

62. Zhang, Z., Yu, Z.-M., Liu, G.-B. & Yao, Y. Magnetictb: a package for tight-binding model of magnetic and non-magnetic materials. *Comput. Phys. Commun.* **270**, 108153 (2022).

63. Zhang, Z. et al. Magnetickp: a package for quickly constructing $k \cdot p$ models of magnetic and non-magnetic crystals. *Comput. Phys. Commun.* **290**, 108784 (2023).

Acknowledgements

Author contributions

W.-T.G. performed the computations, analysis, and writing, Z.H. assisted with the analysis of the results, and J.-M.Z. supervised the execution, analysis the results, reviewed and edited the manuscript.

Competing interests

The authors declare no competing interests.

Additional information

Supplementary information The online version contains supplementary material available at https://doi.org/10.1038/s42005-024-01932-y.

Correspondence and requests for materials should be addressed to Jian-Min Zhang.

Peer review information *Communications Physics* thanks the anonymous reviewers for their contribution to the peer review of this work.

Reprints and permissions information is available at http://www.nature.com/reprints

Publisher's note Springer Nature remains neutral with regard to jurisdictional claims in published maps and institutional affiliations.